The Astrophysical Journal Letters, 988:L51 (14pp), 2025 August 1 https://doi.org/10.3847/2041-8213/adee09

Near-horizon Polarization as a Diagnostic of Black Hole Spacetime

Yehui Hou[1,2,10], Jiewei Huang[2,10], Minyong Guo[3,4], Yosuke Mizuno[1,5,6], and Bin Chen[2,7,8,9]
[1] Tsung-Dao Lee Institute, Shanghai Jiao-Tong University, Shanghai, 201210, People's Republic of China; mizuno@sjtu.edu.cn
[2] School of Physics, Peking University, No. 5 Yiheyuan Rd., Beijing 100871, People's Republic of China; chenbin1@nbu.edu.cn
[3] School of Physics and Astronomy, Beijing Normal University, Beijing 100875, People's Republic of China; minyongguo@bnu.edu.cn
[4] Key Laboratory of Multiscale Spin Physics (Ministry of Education), Beijing Normal University, Beijing 100875, People's Republic of China
[5] School of Physics & Astronomy, Shanghai Jiao-Tong University, Shanghai, 200240, People's Republic of China
[6] Key Laboratory for Particle Physics, Astrophysics and Cosmology (MOE), Shanghai Key Laboratory for Particle Physics and Cosmology, Shanghai Jiao-Tong University, Shanghai, 200240, People's Republic of China
[7] Institute of Fundamental Physics and Quantum Technology, Ningbo University, Ningbo, Zhejiang 315211, People's Republic of China
[8] School of Physical Science and Technology, Ningbo University, Ningbo, Zhejiang 315211, People's Republic of China
[9] Center for High Energy Physics, Peking University, No. 5 Yiheyuan Rd., Beijing 100871, People's Republic of China
Received 2025 May 12; revised 2025 July 9; accepted 2025 July 10; published 2025 July 24

Abstract

A key challenge in imaging supermassive black holes is disentangling gravitational effects from plasma physics in order to accurately determine spacetime properties, particularly black hole spin. In this Letter, we present a fully covariant and rigorous analysis of the synchrotron emission from accreting plasma in the equatorial plane in the stationary, axisymmetric, high-conductivity regime and identify—for the first time—a distinctive near-horizon polarization pattern that remains robust across different flow structures. This pattern arises from strong frame dragging near the event horizon, which induces a degeneracy among plasma flow and magnetic field configurations, yielding a polarization signature determined solely by the spacetime geometry and the observer's inclination. The near-horizon polarization thus offers a clean and precise probe of black hole spin and other fundamental parameters. If future space-based millimeter very long baseline interferometry observations can resolve synchrotron emission originating within approximately 1% of the event horizon radius in M87* or Sgr A*, this universal polarization pattern may become observable.

Unified Astronomy Thesaurus concepts: Astrophysical black holes (98); Black hole physics (159); Kerr black holes (886); Supermassive black holes (1663); Accretion (14); Polarimetry (1278)

1. Introduction

The supermassive black hole images obtained by the Event Horizon Telescope Collaboration have opened an unprecedented window for exploring strong gravitational fields (Event Horizon Telescope Collaboration 2019a, 2019b, 2019c, 2021a, 2021b, 2022a, 2022b, 2024a, 2024b). The strong-field gravity of black holes leaves distinctive imprints on these images (V. I. Dokuchaev & N. O. Nazarova 2020; S. E. Gralla et al. 2020; S. Hadar et al. 2021; L. Medeiros et al. 2022), enabling the investigation of extreme astrophysical environments and allowing constraints to be placed on the black hole's mass, spin, and potential deviations from the Kerr metric based on observational data. In particular, polarimetric observations provide an especially sensitive probe of the horizon-scale environment (M. Moscibrodzka et al. 2017; A. Ricarte et al. 2020; R. Emami et al. 2023). The polarization vector of synchrotron radiation is intrinsically orthogonal to the local magnetic field in the plasma comoving frame (G. B. Rybicki & A. P. Lightman 1979). However, this orthogonality is modified by the rapid accretion flow of the plasma and by gravitational lensing (Z. Gelles et al. 2021), such that the observed polarization pattern encodes information about the magnetic field structure, accretion dynamics, and underlying spacetime geometry.

Magnetized plasmas exhibiting different inflow modes produce distinct magnetic field configurations, which in turn significantly modify the observed polarization morphology (F. H. Vincent et al. 2021; A. Ricarte et al. 2022; A. Chael et al. 2023). By comparing the synthetic images of accretion flows generated from general relativistic magnetohydrodynamics (GRMHD) simulations with observational data, it is possible to qualitatively constrain the underlying magnetic field structure and discriminate between two extreme black hole spin scenarios—rapidly spinning and slowly spinning black holes (D. C. M. Palumbo et al. 2020, 2024; R. Qiu et al. 2023; X. A. Zhang et al. 2025). Nevertheless, the finite angular resolution of telescopes and the complex origins of polarization patterns make it challenging to accurately disentangle gravitational effects from astrophysical ones, limiting our ability to reliably quantify the role of spacetime geometry. Therefore, identifying polarization observables dominated by gravity and insensitive to plasma physics would be highly valuable for both theory and observation.

In this Letter, we show that near-horizon physics offers a promising path forward. In the vicinity of rotating black holes, frame dragging twists both inflowing plasma and magnetic fields into spiral structures (A. Ricarte et al. 2022). Sufficiently close to the horizon, this effect drives a variety of inflow modes toward a predominantly toroidal configuration. We anticipate that such strong frame dragging induces a universal near-horizon polarization (NHP) pattern on the image plane, largely independent of the details of accretion. For sources

[10] These authors contributed equally to this work.

such as M87* and Sgr A*, the inner accretion flow likely resides in a magnetically arrested disk (MAD) state (R. Narayan et al. 2003; A. Tchekhovskoy et al. 2011; Event Horizon Telescope Collaboration 2021b), with emissivity sharply rising toward the horizon (A. Chael et al. 2019, 2021; R. Narayan et al. 2022), enabling photons to escape despite strong gravitational redshift. This makes the NHP pattern potentially observable with future Event Horizon Telescope arrays, especially via space-based very long baseline interferometry (W. Lockhart & S. E. Gralla 2022; D. Ayzenberg et al. 2025; M. D. Johnson et al. 2023; Event Horizon Telescope Collaboration 2024c; H. Jia et al. 2024; M. D. Johnson et al. 2024).

Under the assumptions of stationarity and axisymmetry, we perform a fully covariant analysis of equatorial plasma flows characterized by ideal conductivity and negligible vertical magnetic field component, along with the associated polarized synchrotron emission profile. For the Kerr spacetime, by expanding the flow velocity, magnetic field, and polarized emission in powers of the radial distance from the horizon and employing symmetry-induced lensing and polarization transfer, we derive a general NHP formula. Remarkably, the leading-order NHP pattern depends solely on the spacetime geometry, while the next-to-leading term is influenced by both the spacetime and the field line angular velocity but remains insensitive to the inflow velocity.

We present the analytic NHP pattern on the observer's image plane and demonstrate its strong dependence on black hole spin. Especially for a nearly on-axis observer, the secondary azimuthal Fourier mode β_2 of linear polarization (D. C. M. Palumbo et al. 2020) takes an elegant, model-independent form at leading order,

$$\beta_2 \approx -2\tan^{-1}\left[\frac{a}{\sqrt{4r_+ - a^2}}\right], \tag{1}$$

where a denotes the black hole spin parameter and r_+ is the horizon radius. Our analytic NHP pattern enables direct, nondegenerate spin measurements. Furthermore, we verify that the NHP formula can be directly extended to the Kerr–Newman–Taub–NUT (KNTN) spacetime, suggesting its universality for a broad class of rotating black holes. Throughout this work, we adopt natural units with $GM = c = 1$, where M denotes the black hole mass.

2. The Magnetized Accretion Flow

We begin with a steady-state accretion of a magnetized plasma onto a general stationary, axisymmetric black hole, assuming that the plasma's self-gravity is negligible. The plasma is taken to be perfectly conducting, so that the electric field vanishes in the comoving frame, i.e., $e^\mu = F^{\mu\nu}u_\nu = 0$, where $F^{\mu\nu}$ is the electromagnetic field tensor and u^μ is the plasma four-velocity.

In a stationary and axisymmetric configuration, the electromagnetic field is governed by two conserved quantities along each magnetic field line (or, equivalently, each streamline; K. S. Thorne & D. Macdonald 1982; E. S. Phinney 1984): the stream function ψ, which labels magnetic flux surfaces, and the field line angular velocity Ω_B, which characterizes the rotation of magnetic field lines. In terms of spherical coordinates $\{t, r, \theta, \phi\}$, the magnetic field as measured in the comoving frame can be expressed as

$$\begin{aligned} b^\mu &= -({}^*F)^{\mu\nu}u_\nu \\ &= -\frac{\partial_\theta\psi}{\sqrt{-g}\,u^r}[(u_t + \Omega_B u_\phi)u^\mu + \delta^\mu_t + \Omega_B\delta^\mu_\phi], \end{aligned} \tag{2}$$

where g is the determinant of the metric tensor.

The field line angular velocity Ω_B induces a nonzero electric field in the black hole coordinate frame, enabling energy extraction from black hole rotation via relativistic jets. The extraction efficiency for a Kerr black hole is maximized for $\Omega_B \approx \Omega_H/2$ within the jet region (R. D. Blandford & R. L. Znajek 1977). Numerical simulations further indicate that $\Omega_B \approx 0.2\,\Omega_H$–$0.5\,\Omega_H$ within MADs (A. Tchekhovskoy et al. 2011; J. C. McKinney et al. 2012).

In the MAD regime, the accumulation of magnetic flux near the event horizon generates a strong magnetic pressure that compresses the accretion flow toward the equatorial plane (A. Chael et al. 2019, 2021; A. Ricarte et al. 2022). In this region, the flow becomes predominantly radial, satisfying $|ru^\theta| \ll |u^r|$. The conservation of the stream function simplifies to $u^\mu\partial_\mu\psi \approx u^r\partial_r\psi \approx 0$, implying that $\Psi \equiv \partial_\theta\psi$ can be treated as approximately constant near the equatorial plane (Y. Hou et al. 2024; see Appendix A for details). Under these conditions, Equation (2) reveals a predominantly radial magnetic field structure, with field lines being advected inward by the plasma flow. This behavior is supported by both GRMHD simulations (S. S. Komissarov 2005; A. Tchekhovskoy et al. 2011; J. C. McKinney et al. 2012) and particle-in-cell simulations (K. Parfrey et al. 2019). We do not consider purely circular flows with $u^r = 0$, as they are disfavored by current polarimetric observations (D. C. M. Palumbo 2025).

Notably, in parabolic or more collimated jets extending away from the equatorial plane, the flow velocity and magnetic field tend to develop significant vertical components (A. Tchekhovskoy et al. 2011). Nevertheless, the jet emission is typically subdominant relative to that of the accretion flow. As such, we neglect the jet's emission profile in the present study.

3. Polarized Emission Profile

At millimeter wavelengths, the emission is dominated by (thermal or nonthermal) synchrotron radiation from electrons within the plasma, whose unit-norm polarization vector f^μ is largely perpendicular to the magnetic field (G. B. Rybicki & A. P. Lightman 1979). Thus, without specifying a particular electron distribution, the form of f^μ can be determined by geometric constraints,

$$f^\mu_{(e)} = \frac{\epsilon^{\mu\nu\rho\sigma}u_\nu p_\rho b_\sigma}{\omega\sqrt{b^2_\perp}}, \tag{3}$$

where $\epsilon^{\mu\nu\rho\sigma}$ is the Levi–Civita tensor, p^μ is the photon four-momentum, and $\omega = -u^\mu p_\mu$ is the photon frequency measured in the comoving frame. We have introduced the spatial magnetic field in the comoving frame $b^\mu_\perp = b^\mu - \omega^{-2}(b\cdot p)\,p^\mu_\perp$ to properly normalize f^μ, where $p^\mu_\perp = p^\mu - \omega u^\mu$ is the spatial component of the photon four-momentum. Here, the subscript "(e)" denotes the emission location.

After emission, photons propagate along null geodesics, with their polarization vectors parallel transported along the trajectories. The polarization condition and transport equations are given by $f^\mu p_\mu = 0$, $p^\mu\nabla_\mu p^\nu = p^\mu\nabla_\mu f^\nu = 0$. The polarization

vector admits a gauge freedom $f^{\mu} \rightarrow f^{\mu} + \xi p^{\mu}$, where ξ is an arbitrary constant.

The arrival positions of photons on the image plane of a distant, static observer are described by the image coordinates: $(\alpha, \beta) \propto (-\sin\theta_o p^{\phi}, p^{\theta})$, where θ_o is the observer's inclination angle. The image plane is thus spanned by the tetrad $\{e_{\mu}^{[\alpha]}, e_{\mu}^{[\beta]}\}$ (J. M. Bardeen 1973). The observed polarization pattern can be characterized by the electric vector polarization angle (EVPA) of the arriving photons, computed from the components of f^{μ} projected along the α- and β-directions (Event Horizon Telescope Collaboration 2021b),

$$\chi = \tan^{-1}\left[-\frac{f_{(o)}^{\mu} e_{\mu}^{[\alpha]}}{f_{(o)}^{\mu} e_{\mu}^{[\beta]}}\right], \tag{4}$$

which measures the polarization direction relative to the β-axis. Here, the subscript "(o)" denotes the observer's location.

4. Near-horizon Limit

In this section, we focus on the Kerr geometry to analytically investigate polarization behavior in the vicinity of the event horizon. In Boyer–Lindquist coordinates, the event horizon is defined by the vanishing of the redshift factor,

$$\Delta \equiv r^2 - 2r + a^2 = (r - r_-)(r - r_+) = 0, \tag{5}$$

where a is the black hole spin parameter and $r_{\pm} = 1 \pm \sqrt{1 - a^2}$. The physical event horizon is located at $r = r_+$. Near the horizon, $\Delta \approx (r_+ - r_-)\delta r$, with $\delta r = r - r_+$, allowing the use of the redshift factor Δ as a measure of the radial distance to the horizon.

In the near-horizon limit $\Delta \rightarrow 0$, all relevant quantities are expanded as power series in Δ on the equatorial plane. Without loss of generality, we set $u^{\theta} = 0$ and hold u_t, u_{ϕ} constant during the expansion. The components of the flow velocity are then given by

$$\begin{aligned} u^t &= -\frac{4Y}{\Delta} - \left(1 + \frac{2}{r_+}\right)u_t + \frac{a u_{\phi}}{r_+^2(r_+ - 1)} + \mathcal{O}(\Delta), \\ u^r &= -\frac{2|Y|}{r_+} + \mathcal{O}(\Delta), \quad u^{\theta} = 0, \\ u^{\phi} &= -\frac{2aY}{r_+\Delta} + \frac{a u_t + u_{\phi}}{r_+^2(r_+ - 1)} + \mathcal{O}(\Delta), \end{aligned} \tag{6}$$

where $Y = u_t + \Omega_H u_{\phi}$, $\Omega_H = a/(2r_+)$ is the angular velocity of the Kerr horizon. The radial velocity u^r is determined by the normalization $u^{\mu}u_{\mu} = -1$, and we choose $u^r < 0$ to describe accreting plasma. To leading order, $u^{\phi}/u^t \approx \Omega_H$ and $u^r/u^t \approx \sigma_Y a^{-1}\Omega_H\Delta$, where σ_Y denotes the sign of Y. For plunging matter, $\sigma_Y < 0$, consistent with the second law of black hole thermodynamics (S. Chandrasekhar 1985); specifically, a test particle with $Y > 0$ cannot classically reach the horizon. In Equation (6), u_t and u_{ϕ} are two free functions of r outside the horizon. They constitute the 2 degrees of freedom of equatorial plasma motion and determine the specific inflow structure.

The near-horizon expansion of the magnetic field, as given by Equation (2), reads

$$\begin{aligned} b^t &= \frac{2\Psi}{r_+\Delta}(u_t + \Omega_B u_{\phi}) + \mathcal{O}(1), \\ b^r &= -\frac{\Psi}{r_+^2}(u_t + \Omega_B u_{\phi}), \quad b^{\theta} = 0, \\ b^{\phi} &= \frac{\Psi a}{r_+^2\Delta}(u_t + \Omega_B u_{\phi}) + \mathcal{O}(1). \end{aligned} \tag{7}$$

The ratio $b^{\phi}/b^r \approx -a\Delta^{-1}$ reveals a highly toroidal magnetic field structure near the horizon (A. Ricarte et al. 2022). The vanishing of b^{θ} arises from the assumption that $u^{\theta} = 0$—since the vertical velocity is rather small compared to the radial one near the equatorial plane, according to Equation (2), we have $r|b^{\theta}| \ll |b^r|$.

In the Kerr spacetime, photon trajectories are characterized by three constants of motion: the energy $\mathcal{E} = -p_t$, the angular momentum $\mathcal{L} = p_{\phi}$, and the Carter constant $\mathcal{Q} = p_{\theta}^2 + a^2\mathcal{E}^2\cos^2\theta + \mathcal{L}^2\cot^2\theta$. The r, θ components of the photon momentum are determined by effective potentials (B. Carter 1968). By expanding the photon four-momentum and employing Equations (6) and (7), the near-horizon expansion for the polarization vector at the emission point is

$$\begin{aligned} Xf_{(e)}^t &= \frac{4\sigma_\theta\sqrt{\eta}}{\Delta}(\Omega_B - \Omega_H) + \frac{\sigma_\theta\sqrt{\eta}}{r_+}(r_+ + 2)\Omega_B \\ &\quad + \frac{a\sigma_\theta\sqrt{\eta}}{r_+^2(r_+ - 1)} + \mathcal{O}(\Delta), \\ Xf_{(e)}^r &= \frac{2\sigma_\theta\sqrt{\eta}}{r_+}(\Omega_B - \Omega_H) + F_r\Delta + \mathcal{O}(\Delta), \\ Xf_{(e)}^{\theta} &= -4\frac{(\Omega_H\lambda - 1) - \sigma_r|\Omega_H\lambda - 1|}{\Delta}(\Omega_B - \Omega_H) \\ &\quad + F_{\theta} + \mathcal{O}(\Delta), \\ Xf_{(e)}^{\phi} &= \frac{2a\sigma_\theta\sqrt{\eta}}{r_+\Delta}(\Omega_B - \Omega_H) \\ &\quad + \frac{\sigma_\theta\sqrt{\eta}}{r_+^2(r_+ - 1)}(1 - a\Omega_B) + \mathcal{O}(\Delta), \end{aligned} \tag{8}$$

where $X = -\Psi^{-1}\mathcal{E}^{-1}\omega\sqrt{-g\ b_{\perp}^2}$; σ_r, σ_θ denote the signs of p_r and p_{θ}; and $\lambda \equiv \mathcal{L}/\mathcal{E}$, $\eta \equiv \mathcal{Q}/\mathcal{E}^2$ are the photon impact parameters, which specify the emission direction (C. T. Cunningham & J. M. Bardeen 1973). We restrict to $\eta > 0$, corresponding to light rays that can reach the equatorial plane.

The leading-order terms in Equation (8) are all proportional to $(\Omega_B - \Omega_H)$ and do not explicitly depend on u^{μ}. Nevertheless, since the prefactor X depends on u^{μ}, the leading-order polarization vector retains an implicit dependence on the flow velocity. The terms F_r and F_{θ} in Equation (8) are functions of the flow velocity, but their explicit forms are lengthy and omitted here for brevity.

5. The NHP Formula

Since the Kerr spacetime is of Petrov type D (A. Z. Petrov 1954), there exists a conserved quantity associated with the parallel transport of the polarization vector along a null geodesic: the complex Penrose–Walker constant

(M. Walker & R. Penrose 1970),

$$\kappa \equiv \kappa_1 + i\kappa_2 = (r - ia\cos\theta)(\mathcal{A} - i\mathcal{B}),$$
$$\mathcal{A} = 2p^{[t}f^{r]} + 2a\sin^2\theta p^{[r}f^{\phi]},$$
$$\mathcal{B} = 2\sin\theta[(r^2 + a^2)p^{[\phi}f^{\theta]} - ap^{[t}f^{\theta]}], \quad (9)$$

where κ_1, κ_2 denote the real and imaginary parts of κ, respectively. According to Equation (9), the parallel transport of the polarization vector reduces to an algebraic problem: its 2 degrees of freedom, $\{f^{\alpha}_{(o)}, f^{\beta}_{(o)}\}$, can be expressed in terms of κ_1 and κ_2, which are determined by $f^{\mu}_{(e)}$ at the emission point.

Using the near-horizon expansion for $f^{\mu}_{(e)}$ (Equation (8)) and the expansion of the photon four-momentum, we find that the ratio

$$z \equiv \frac{\kappa_1}{\kappa_2} = z_0 + z_1\Delta + \mathcal{O}(\Delta^2) \quad (10)$$

is independent of the flow velocity up to next-to-leading order. Here, we introduce the following expressions:

$$z_0 = \frac{\sigma_\theta\sqrt{\eta}}{\lambda - a},$$
$$z_1 = \Omega_H^2\frac{(1 - a\Omega_B)}{(\Omega_H - \Omega_B)}\frac{\sigma_\theta(1 + z_0^2)\sqrt{\eta}}{2a^2(\Omega_H\lambda - 1)}. \quad (11)$$

It should be noted that Equation (10) is valid below the superradiant bound, i.e., $\lambda \leqslant 1/\Omega_H$, which ensures that photons from near-horizon emission with positive energy (and thus observational relevance) satisfy this condition (G. Compère et al. 2022).

We then propagate the near-horizon expansion for $f^{\mu}_{(e)}$ to the observer's image plane to obtain the NHP pattern. In the Kerr spacetime, the image coordinates of the arriving photons are related to the impact parameters (J. M. Bardeen 1973): $\alpha = -\lambda(\sin\theta_o)^{-1}$, $\beta^2 = \eta + (a^2 - \alpha^2)\cos^2\theta_o$. From Equations (4) to (9), the distribution of the EVPA (Equation (4)) on the image plane takes the form of E. Himwich et al. (2020),

$$\chi = \tan^{-1}\left(\frac{\mu z - \beta}{\beta z + \mu}\right), \quad \mu = -(\alpha + a\sin\theta_o). \quad (12)$$

Combining Equations (10) and (12), we obtain the near-horizon EVPA as

$$\chi = -\tan^{-1}\left(\frac{\beta}{\mu}\right) + \tan^{-1}z_0 + \frac{z_1\Delta}{1 + z_0^2} + \mathcal{O}(\Delta^2). \quad (13)$$

In this expansion for χ, the leading-order term depends only on the black hole spin parameter and the image coordinates (α, β).[11] The next-to-leading-order term is determined by the spin parameter, image coordinates, and field line angular velocity Ω_B. Therefore, the near-horizon EVPA distribution on the image plane (Equation (13)) is independent of the flow structure, being determined solely by the spacetime geometry and the magnetic field rotation. In particular, this result highlights a unique imprint of the black hole spin on the NHP. Note that when using Equation (13), a modulus should be applied to χ to confine it to $[-\pi/2, \pi/2]$, since the arctangent sum may exceed this range.

[11] It is well established that the first-order geodesic equations in the r- and θ-directions in the Kerr spacetime allow the emission-image mapping to be expressed via geodesic integrals, yielding $\Delta = \Delta(\alpha, \beta, a, \theta_o)$ (K. Beckwith & C. Done 2005; S. E. Gralla & A. Lupsasca 2020).

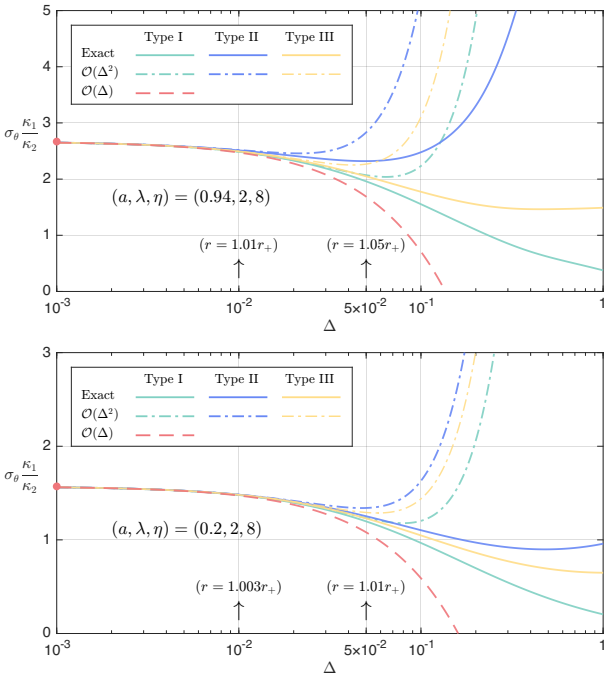

Figure 1. Comparison of the ratio z up to the next-to-leading order (Equation (10)) with the exact value under different inflow modes, under $a = 0.94$ (top) and $a = 0.2$ (bottom). We have chosen a typical direction for the emitted photons with $(\lambda, \eta) = (2, 8)$, and the field line angular velocity is set to $\Omega_B = 0.3\Omega_H$. For results of other parameter choices, see Appendix B.

To assess the convergence radius of the near-horizon expansion, we compare $z_0(a, \lambda, \eta) + z_1(a, \lambda, \eta, \Omega_B)\Delta$ from Equation (10) with the exact value $z(a, \Delta, \lambda, \eta, \Omega_B, u^{\mu})$ for different inflow models characterized by distinct u_t and u_ϕ: freefall (type I), plunging from the prograde innermost stable circular orbit (ISCO; type II), and the fit from the MAD simulation (type III; A. Chael et al. 2021). The comparison is shown in Figure 1, where representative values of λ, η and Ω_B are chosen (see Appendix B for results for a broader parameter space). As shown in Figure 1, the expansion in Equation (10) up to next-to-leading order in the redshift factor is accurate for $0 \leqslant \Delta \lesssim 10^{-2}$ (corresponding to $r = 1.01r_+$ for $a = 0.94$ and $r = 1.003r_+$ for $a = 0.2$) across all three flow models. Inclusion of the next-to-next-to-leading-order term further improves the accuracy only in a very narrow region around $\Delta \simeq 5 \times 10^{-2}$ (corresponding to $r = 1.05r_+$ for $a = 0.94$ and $r = 1.01r_+$ for $a = 0.2$).

In addition, the derivation of Equation (13) in the present study is based on a radial inflow, assuming $b^{\theta} \propto u^{\theta} = 0$, in accordance with MADs. However, we have numerically confirmed that introducing a small but nonzero vertical component preserves the leading-order result as given in Equation (13); namely, $z_0 = \sigma_\theta\sqrt{\eta}(\lambda - a)^{-1}$ still holds. However, the presence of b^{θ} modifies the subleading-order term, and u^{θ} enters into the expression for z_1, rendering it more complex. The full expression is omitted for brevity.

6. NHP on the Image Plane

In Figure 2, we show the direct projection of the event horizon onto the image plane, together with the corresponding leading-order NHP pattern, i.e., $\chi = -\tan^{-1}(\beta/\mu) + \tan^{-1}z_0$,

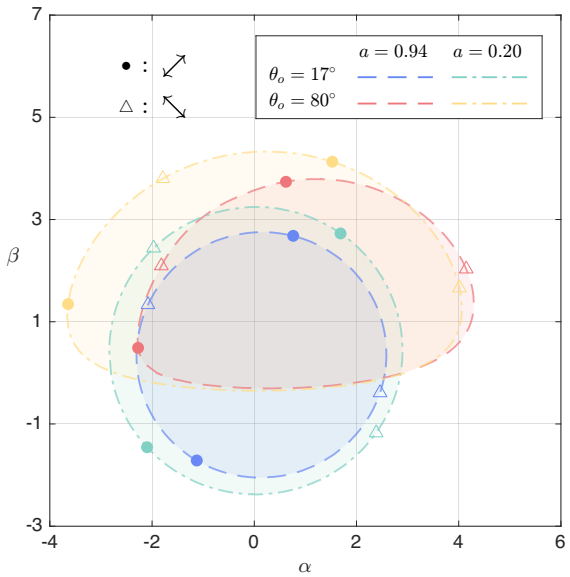

Figure 2. The dashed lines represent the projected event horizons. The circles mark the locations where $\chi = -\pi/4$, and the triangles mark the locations where $\chi = \pi/4$. The projection of the black hole's rotation direction onto the screen aligns with the β-axis.

for various black hole spins and inclination angles. For clarity, only those image points satisfying $\chi = \pm\pi/4$ are indicated, highlighting their dependence on both the spin and the inclination angle. Since a and θ_o affect the leading-order NHP in distinct and nondegenerate ways, their respective contributions can be disentangled from the EVPA distribution.

To better characterize the NHP pattern, we introduce the net EVPA, $\chi_{\rm net} \equiv \chi - \varphi$, which indicates the angle between the polarization vector and the vector from the origin to the image point. Here, $\varphi = -\tan^{-1}(\alpha/\beta)$ is the polar angle on the image plane, measured with respect to the β-axis. For small inclination angles, the polarization is nearly axisymmetric with respect to the line of sight, and we have $2\chi_{\rm net} \approx \beta_2$, where β_2 is the second azimuthal Fourier mode of the linear polarization at fixed angular radius (Event Horizon Telescope Collaboration 2021a, 2021b, 2024a), serving as a good indicator of the overall polarization structure.

Figure 3 displays the variation of the net EVPA along the projected event horizon for different values of a and θ_o. It is evident that the inclination angle has a significant impact on the variation of $\chi_{\rm net}$ along the horizon contour, while increasing the spin results in an overall downward shift of $\chi_{\rm net}$. For high inclination ($\theta_o = 80°$), $\chi_{\rm net}$ in the lower half of the image plane is largely insensitive to the spin, whereas the upper half remains sensitive to changes in spin. In contrast, for low inclination ($\theta_o = 17°$), as favored by M87* shadow measurements (Event Horizon Telescope Collaboration 2019a, 2019b, 2019c), the entire NHP pattern is sensitive to the spin parameter: as a increases from 0.2 to 0.94, $\chi_{\rm net}$ shifts downward by nearly 20°. These results demonstrate that the NHP provides a potentially powerful and model-independent method for measuring black hole spin.

In the case of small inclination angles, Equation (12) can be expanded in terms of θ_o to yield an explicit expression for the NHP. In particular, for $\theta_o = 0°$, the leading-order net EVPA takes a particularly simple form: $\chi_{\rm net} = -\tan^{-1}(a/\sqrt{(\rho_+)^2 - a^2})$, where ρ_+ denotes the angular radius of the projected event horizon. Combining this formula with the semianalytical relation

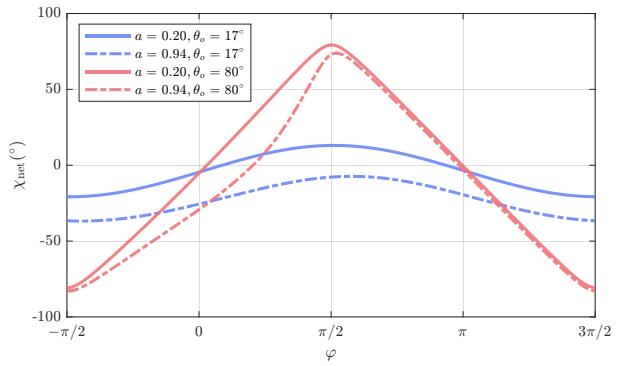

Figure 3. The leading-order net EVPA along the projected event horizon as φ changes, under different spins and inclination angles. We have taken the modulus of $\chi_{\rm net}$ to bring it within the range of $[-\pi/2, \pi/2]$.

$\rho_+ \approx 2\sqrt{r_+}$ (A. Chael et al. 2021) yields the explicit expression for β_2 given in Equation (1). Further details are provided in Appendix C.

7. Summary and Discussion

Assuming a stationary, axisymmetric, highly conducting accreting flow in the equatorial plane with polarized synchrotron emission, we explicitly showed that black hole spin imprints a characteristic polarization pattern via strong frame dragging near the horizon. In the near-horizon expansion of the Kerr spacetime, the leading-order NHP depends only on the spacetime geometry and observer's inclination, remaining independent of the inflow structure or electron distribution. This property offers a novel and robust diagnostic of black hole spin. The next-to-leading-order term incorporates the field line angular velocity, indicating that polarimetric observations just outside the horizon can reveal black hole–magnetic field coupling and potentially the origin of jets. We further extended the analysis to the KNTN spacetime (Appendix D), suggesting the broader applicability of the NHP formula.

Although derived under the assumptions of global stationarity and axisymmetry, the NHP formula (Equation (13)) characterizes the distribution of the near-horizon EVPA rather than total linear polarization degree. Thus, in turbulent accretion flows, the NHP can partially survive in the regions where turbulence is weak and the plasma and magnetic field remain locally coupled via Equation (2). Moreover, even if instantaneous turbulent flows may not display polarization patterns consistent with the NHP prediction, time-averaging can suppress fluctuations and recover underlying structures, offering a potential avenue for testing the formula in GRMHD simulations. In the MAD regime, emissivity is greatly enhanced near the event horizon, counteracting gravitational redshift and suggesting that the NHP may be detectable with future high-resolution observations (D. Ayzenberg et al. 2025; M. D. Johnson et al. 2023, 2024; Event Horizon Telescope Collaboration 2024c).

The present study focuses on accretion flow emission confined to the equatorial plane, excluding the contributions from off-equatorial regions such as the jet sheath. Our preliminary study suggests that for finite deviations from the equator, the NHP exhibits flow-mode dependence when the emitting region is geometrically thin. Extending the analysis to include jet emission is a goal for future work. Additionally, in

the finite-conductivity regime, the coupling between flow velocity and the magnetic field becomes more complex than Equation (2), necessitating detailed plasma modeling, including the treatment of ion and electron drift currents—an issue we also intend to address in future studies.

We did not account for Faraday depolarization (A. Ricarte et al. 2020). However, since the NHP formula is achromatic and purely geometric, and the rotation measure near M87* and Sgr A* is nearly constant, future broadband and multi-frequency polarimetric observations will allow effective separation of Faraday effects and recovery of the intrinsic NHP pattern. Additionally, at sufficiently high frequencies, Faraday rotation becomes negligible, further simplifying the interpretation.

Acknowledgments

The work is partly supported by NSFC grant Nos. 12205013 and 12275004. Y.M. is supported by the National Key R&D Program of China (grant No. 2023YFE0101200), the National Natural Science Foundation of China (grant No. 12273022), and the Shanghai Municipality Orientation Program of Basic Research for International Scientists (grant No. 22JC1410600).

Appendix A
Magnetic Field Structure in the Accreting Plasma

The electromagnetic field plays a crucial role in magneto-hydrodynamics (MHD). The electric and magnetic fields measured in the plasma comoving frame are defined as

$$e^\mu = u_\nu F^{\mu\nu}, \quad b^\mu = -u_\nu (*F)^{\mu\nu}, \tag{A1}$$

where $F^{\mu\nu}$ is the electromagnetic tensor, $(*F)^{\mu\nu}$ is the dual tensor, and u^μ is the flow four-velocity. Using the definitions of e^μ and b^μ, the field strength tensor and its dual can be expressed as

$$\begin{aligned} F^{\mu\nu} &= u^\mu e^\nu - u^\nu e^\mu + \epsilon^{\mu\nu\alpha\beta} u_\alpha b_\beta, \\ (*F)^{\mu\nu} &= b^\mu u^\nu - b^\nu u^\mu - \epsilon^{\mu\nu\alpha\beta} e_\alpha u_\beta, \end{aligned} \tag{A2}$$

where $\epsilon^{\mu\nu\alpha\beta}$ is the Levi–Civita tensor in curved spacetime. The electromagnetic energy–momentum tensor can be rewritten in terms of the electric and magnetic fields as (J. C. McKinney 2006)

$$T^{\mu\nu}_{\rm EM} = \left(u^\mu u^\nu + \frac{1}{2} g^{\mu\nu}\right)(e^2 + b^2) - e^\mu e^\nu - b^\mu b^\nu \,. \tag{A3}$$

In the study of GRMHD around black holes, it is convenient to introduce the so-called pseudoelectromagnetic fields, defined as the contractions of the electromagnetic tensor and dual tensor with the time-like Killing vector,

$$E^\mu = (dt)_\nu F^{\mu\nu} = F^{t\mu}, \quad B^\mu = -(dt)_\nu (*F)^{\mu\nu} = -(*F)^{t\mu} \,. \tag{A4}$$

These pseudofields do not belong to physical fields measured by any observer, but they are widely used in GRMHD due to their simplified form and computational convenience in stationary spacetimes. In fact, compared to the pseudofields, the electromagnetic fields measured in the spacetime normal observer differ only by a lapse function (S. S. Komissarov 2004). Using Equation (A4), one can derive the transformation relations between the pseudofields and the magnetic field measured in the comoving frame:

$$E^\mu = F^{t\mu} = -\epsilon^{t\mu\alpha\beta} b_\alpha u_\beta, \quad B^\mu = b^{[\mu} u^{t]}, \tag{A5}$$

$$b^t = g_{i\mu} B^i u^\mu, \quad b^i = \frac{B^i + B^t u^i}{u^t}. \tag{A6}$$

In our study, we are interested in steady-state, axisymmetric plasma configurations embedded in a steady-state, axisymmetric spacetime. In spherical coordinates, the spacetime line element takes

$$ds^2 = g_{tt} dt^2 + 2 g_{t\phi} dt d\phi + g_{\phi\phi} d\phi^2 + g_{rr} dr^2 + g_{\theta\theta} d\theta^2. \tag{A7}$$

The physical quantities vary only in the (r, θ) plane, and we henceforth denote this as the poloidal plane and refer to r, θ as the poloidal coordinates. For accreting plasma with high enough conductivity, the electric field within the plasma frame is zero, $F^{\mu\nu} u_\nu = 0$. This is also called the ideal MHD condition, widely used in both theoretical studies and numerical simulations. In the following, we would like to derive the field structure by imposing symmetry requirements and the ideal MHD condition. Since the electromagnetic tensor only depends on r, θ, the azimuthal component of the electric field vanishes,

$$E^\phi = F^{t\phi} = [g^{tt} g^{\phi\phi} - (g^{t\phi})^2] F_{t\phi} = 0, \tag{A8}$$

where $F_{t\phi}$ is evaluated as $F_{t\phi} = \partial_t A_\phi - \partial_\phi A_t = 0$, with $A_\mu(r, \theta)$ the gauge potential. Applying the ideal MHD condition in the t-direction, we obtain the following orthogonality:

$$F^{ti} u_i = E^P u_P = 0 \,. \tag{A9}$$

Here and thereafter, we label the poloidal coordinates r, θ by the index P. Meanwhile, the ideal MHD condition in the ϕ- (toroidal) direction leads to $F_{\phi\mu} u^\mu = F_{\phi P} u^P = 0$, which can be expressed in terms of B^P:

$$B^r u^\theta - B^\theta u^r = 0 \,. \tag{A10}$$

The above equation means that the magnetic field line is aligned with the streamline within the poloidal plane. The exceptional case is $u^r = u^\theta = 0$, where the electromagnetic field cannot be determined by ideal MHD alone; additional conditions are required. For example, at the launch point of a jet, the magnetic field is determined by the smoothness near the launch point. Moreover, using the gauge potential, we have

$$B^r = \frac{\partial_\theta A_\phi}{\sqrt{-g}}, \quad B^\theta = -\frac{\partial_r A_\phi}{\sqrt{-g}}, \quad u^P \partial_P A_\phi = 0, \tag{A11}$$

where g is the determinant of the spacetime metric. The third equation comes from Equation (A10), meaning that A_ϕ is conserved along the fluid streamlines. In fact, $A_\phi(r, \theta)$ marks the magnetic flux enclosed by a circular loop of radius r and polar angle θ, and thus we denote it as the stream function of the magnetized plasma, $\psi \equiv A_\phi(r, \theta)$.

The ideal MHD condition in the poloidal directions leads to

$$\begin{aligned} g_{rr} E^r &= g^{tt} v^\theta F_{r\theta} + (g^{tt} v^\phi - g^{t\phi}) F_{r\phi}, \\ g_{\theta\theta} E^\theta &= g^{tt} v^r F_{\theta r} + (g^{tt} v^\phi - g^{t\phi}) F_{\theta\phi}, \end{aligned} \tag{A12}$$

where we have introduced $v^\mu \equiv u^\mu / u^t$. Multiply the first equation of Equation (A12) by B^r and the second equation by

B^θ, then add the two resulting equations together to obtain

$$g_{PP}E^P B^P = 0; \tag{A13}$$

hence, the pseudoelectric field and pseudomagnetic field are orthogonal within the poloidal plane. Moreover, applying the index lowering relation, we have $g^{tt}F_{tP} = (g_{PP}E^P + g^{t\phi}F_{P\phi})$. Combined with Equation (A13), we can deduce $F_{t\theta}F_{r\phi} = F_{tr}F_{\theta\phi}$. It is convenient to define the following "angular velocity":

$$\Omega_B \equiv \frac{F_{tP}}{F_{P\phi}}, \quad P = r, \theta\,. \tag{A14}$$

Note that this angular velocity does not characterize the local twisting of the field lines, i.e., the ratio of the toroidal to poloidal components of the magnetic field. Instead, it represents the global rotation of a magnetic field line around the black hole. Thus, Ω_B is often called the field line angular velocity. We can rewrite the pseudoelectric field as

$$E^P = -\left(\frac{g^{PP}\sqrt{-g}}{g^{tt}}\right)\left(\Omega_B - \frac{g^{t\phi}}{g^{tt}}\right)\tilde{\epsilon}_{PP'}B^{P'}\,. \tag{A15}$$

It becomes clear that the pseudoelectric field is induced by both the field line rotation and the spacetime frame dragging, represented by $g^{t\phi}$. Then, we would like to explore the conservation law for Ω_B. The Bianchi identity of the electromagnetic field in the ϕ-direction gives $\partial_r F_{\theta t} + \partial_\theta F_{tr} = 0$ (in the stationary and axisymmetric case, $\partial_{[r}F_{\theta\phi]} = \partial_{[t}F_{\theta\phi]} = \partial_{[t}F_{r\phi]} = 0$ gives a trivial result). Then, using Equation (A14), we arrive at

$$F_{r\phi}\partial_\theta\Omega_B - F_{\theta\phi}\partial_r\Omega_B + (\partial_\theta F_{r\phi} - \partial_r F_{\theta\phi})\Omega_B = 0\,. \tag{A16}$$

Since $F_{P\phi} = \partial_P\psi$, the last term on the left-hand side of the equation vanishes automatically. Therefore, we have

$$B^P\partial_P\Omega_B = 0, \tag{A17}$$

which indicates that Ω_B is conserved along a field line within the poloidal plane. By using the definition of Ω_B and the ideal MHD condition in the poloidal directions, the toroidal component B^ϕ can be written as

$$B^\phi = (u^\phi - \Omega_B u^t)\frac{B^P}{u^P}\,. \tag{A18}$$

Finally, we would like to consider the ideal-MHD-induced field close to the equatorial plane, aiming to capture the feature of the magnetic field within the accretion disk. Strictly at the equatorial plane, the condition $u^\theta = 0$ holds to ensure a steady state without accumulation. If we further impose a reflection symmetry about the equatorial plane, the electromagnetic field at the equatorial plane satisfies $B^r = 0$ and $E^\theta = 0$. Therefore, from Equation (A10), we know that if $B^\theta \neq 0$, then $u^r = 0$. In this case, from the expression of B^ϕ (Equation (A18)), we find that

$$\Omega_B = \frac{u^\phi}{u^t} = \Omega_m, \tag{A19}$$

where Ω_m is the flow angular velocity. Thus, the vertical magnetic field lines are anchored in the equatorial matter and corotate with it. This condition is widely used in the study of jets induced by magnetized accretion flow, namely, the Blanford–Payne jet (R. D. Blandford & D. G. Payne 1982). The magnetic field measured in the plasma frame has a vertical structure in the poloidal plane,

$$b^t = B^\phi_{\rm ver}u_\phi, \quad b^r = 0, \quad b^\theta = \frac{B^\theta_{\rm ver}}{u^t}\,, \quad b^\phi = -B^\phi_{\rm ver}u_t, \tag{A20}$$

where $B^\theta_{\rm ver}$, $B^\phi_{\rm ver}$ are undetermined functions of r. The left panel in Figure 4 provides a representative structure of the vertical magnetic field. However, this vertical structure is not well applicable to the advection-dominated accretion flow very close to a supermassive back hole, where the accretion matter is dilute and inward flow is strong, with a large radial velocity u^r.

If $B^\theta = 0$ at the equatorial plane, the accretion rate is no longer required to vanish. In this case, using Equations (A9) and (A18), we have $E^r = 0$ and $B^\phi = 0$, respectively. Hence, for a nonzero accretion rate, the electromagnetic field should be zero at the equatorial plane, $E^\mu|_{\theta=\pi/2} = B^\mu|_{\theta=\pi/2} = 0$. Slightly above/below the equatorial plane, we have $u^\theta, B^\theta, E^r \approx 0$, but $u^r, B^r, E^\theta \neq 0$, corresponding to a split-monopole-like configuration near the equatorial plane, with a radial structure in the poloidal plane. With the expressions for the pseudomagnetic field (Equations (A11) and (A18)) and the relation Equation (A5), the magnetic field measured in the comoving frame takes the form of

$$b^\mu = -\frac{\partial_\theta\psi}{\sqrt{-g}\,u^r}[(u_t + \Omega_B u_\phi)u^\mu + \delta^\mu_t + \Omega_B\delta^\mu_\phi]\,. \tag{A21}$$

Very close to the equatorial plane, we have $u^\mu\partial_\mu\psi \approx u^r\partial_r\psi = 0$. Thus, ψ is the function of θ only. As long as the variation of ψ with respect to θ is not too sharp (a natural case, as is shown in S. S. Komissarov 2005), we can safely replace $\partial_\theta\psi$ by the averaged value,

$$\bar{\Psi} \equiv \frac{1}{\delta\theta}\int_{\pi/2-\delta\theta}^{\pi/2}\partial_\theta\psi d\theta = \frac{\psi(\pi/2+\delta\theta) - \psi(\pi/2)}{\delta\theta}, \tag{A22}$$

where $\delta\theta$ denotes the thickness of the accretion disk. For the MAD simulation, the accretion matter is highly concentrated on the equatorial plane (see Figure 3 in S. S. Komissarov 2005; Figure 2 in A. Chael et al. 2019; Figure 4 in A. Chael et al. 2021), and we have $\delta\theta \ll \pi/2$. The solution (Equation (A21)) can well capture the magnetic field in the near-horizon part of MAD, as is demonstrated in various numerical simulations (S. S. Komissarov 2005; A. Tchekhovskoy et al. 2011; J. C. McKinney et al. 2012; K. Parfrey et al. 2019; R. Narayan et al. 2022).

In fact, for a given vertical magnetic field, the accretion process will generally lead to a split-monopole-like configuration near the black hole (more precisely, within the ergosphere). The right panel in Figure 4 provides a representative magnetic field within simulated quasi-steady accretion flows. We see that far away from the black hole, the field line is across the equatorial plane. Near the black hole, the field lines are connected to the event horizon and appear as a deformed split monopole. Close to the equatorial plane, we have $b^\theta, B^\theta \approx 0$, and the magnetic field is well described by Equation (A21). At the equatorial plane, a current sheet forms at the equatorial plane, where magnetic reconnection occurs and the magnetic field structure gets turbulent (S. S. Komissarov 2005). Theoretically, this type of configuration genuinely corresponds to the saturated state of magnetic flux threading the horizon.

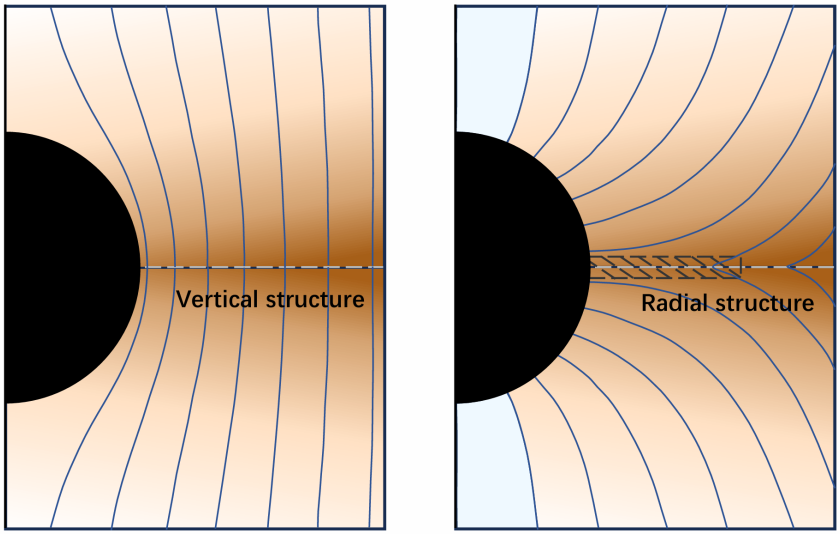

Figure 4. Schematic diagram for the magnetic field topologies outside the black hole, within the poloidal plane. The dashed gray line denotes the location of the equatorial plane. Left: vertical magnetic field across the equatorial plane. Right: radial magnetic field. The hatched square region denotes the area of concentrated matter that predominantly contributes to the synchrotron radiation. The light blue regions near the polar axis indicate the jet regions of quasi-electromagnetic vacuum.

Magnetic field lines connected to the event horizon are dragged by the rotating black hole. In regions very close to the polar axis, the magnetic energy density is much higher than the plasma energy density, making the force-free approximation applicable (K. S. Thorne & D. Macdonald 1982; light blue regions in Figure 4). In such cases, if the field line angular velocity Ω_B is less than the black hole's angular velocity Ω_H, energy extraction can occur, resulting in the formation of an electromagnetic jet. In the jet region, Ω_B tends to approach $\Omega_H/2$ to enable efficient energy extraction (A. Tchekhovskoy et al. 2010).

In regions near the equatorial plane where field lines still connect to the event horizon, Ω_B is jointly determined by the black hole's spin and the inertia of the plasma and typically lies between 0.2 and 0.5 (A. Tchekhovskoy et al. 2011). For field lines that do not connect to the event horizon but instead to the equatorial disk (such as all the field lines in Figure 1 or the outer ones in Figure 2), their angular velocity Ω_B is largely controlled by the plasma's own rotation (J. C. McKinney et al. 2012).

The rotation of magnetic field lines imprints characteristic signatures on the intrinsic polarization profiles of the emission, producing observable effects in accretion and jet polarimetry (Z. Gelles et al. 2025). As demonstrated in the main text for the NHP pattern, the influence of Ω_B enters only at subleading order (see Equation (11)), indicating that its variations are effectively suppressed at the horizon. Nevertheless, even slight departures from the horizon can induce polarization responses that are sensitive to changes in Ω_B. Future high-precision observations may offer a means to distinguish different values of Ω_B within the emitting plasma.

Appendix B
Examination of the Applicability of the NHP Formula

The polarized emission profile, denoted by f_e^μ, is governed by several key physical parameters: the black hole spin a, the plasma inflow four-velocity $u^\mu(r)$, the magnetic field $b^\mu(r)$, and the emission direction characterized by the impact parameters λ, η. In a highly conducting plasma with a nonzero accretion rate, the magnetic field is not an independent degree of freedom but is instead constrained by the plasma motion and the field line angular velocity Ω_B, as specified by Equation (A21). When this emission is projected onto the observer's image plane, it gives rise to a distribution of the EVPA. Utilizing the Penrose–Walker constant, the EVPA χ can be expressed as

$$\chi(a, \theta_o, \alpha, \beta, \Omega_B, u^\mu) = \tan^{-1}\left(\frac{\beta}{\alpha + a\sin\theta_o}\right) + \tan^{-1} z(a, \theta_o, \alpha, \beta, \Omega_B, u^\mu), \tag{B1}$$

where z denotes the ratio of the real to imaginary parts of the Penrose–Walker constant. Notably, plasmas characterized by different inflow profiles and field line angular velocities will exhibit distinct polarization signatures, primarily through the second term in Equation (B1). To compute the explicit value of the EVPA, one must first evaluate z as a function of the impact parameters λ, η, r, and the local plasma properties $u^\mu(r)$, Ω_B at the emission point. Then, we apply the lensing formalism in the Kerr spacetime, which provides an exact mapping between the emission position and the image plane coordinates (α, β) (S. E. Gralla & A. Lupsasca 2020). Specifically, the impact parameters are directly related to α, β by definition, while the radius of the emission point, encoded in the redshift factor $\Delta = (r - r_+)(r - r_-)$, can be expressed as a function of λ, η using the so-called "inverse formula" (S. E. Gralla & A. Lupsasca 2020).

Focusing on the near-horizon region, the main text demonstrates that the NHP pattern exhibits a remarkable insensitivity to variations in the inflow modes. In particular, the leading-order term in the near-horizon expansion of z with respect to Δ is determined solely by the spacetime geometry, while the next-to-leading-order term depends only on the background spacetime and the angular velocity Ω_B (see Equations (11) and (13)). To assess the convergence of the NHP approximation, we compare the flow-independent expression for the EVPA given in Equation (13) with the EVPAs computed from several distinct inflow models. Specifically, we consider the following three representative inflow configurations: (type I) freefall from rest at infinity, (type II) plunging from the prograde ISCO, and (type III)

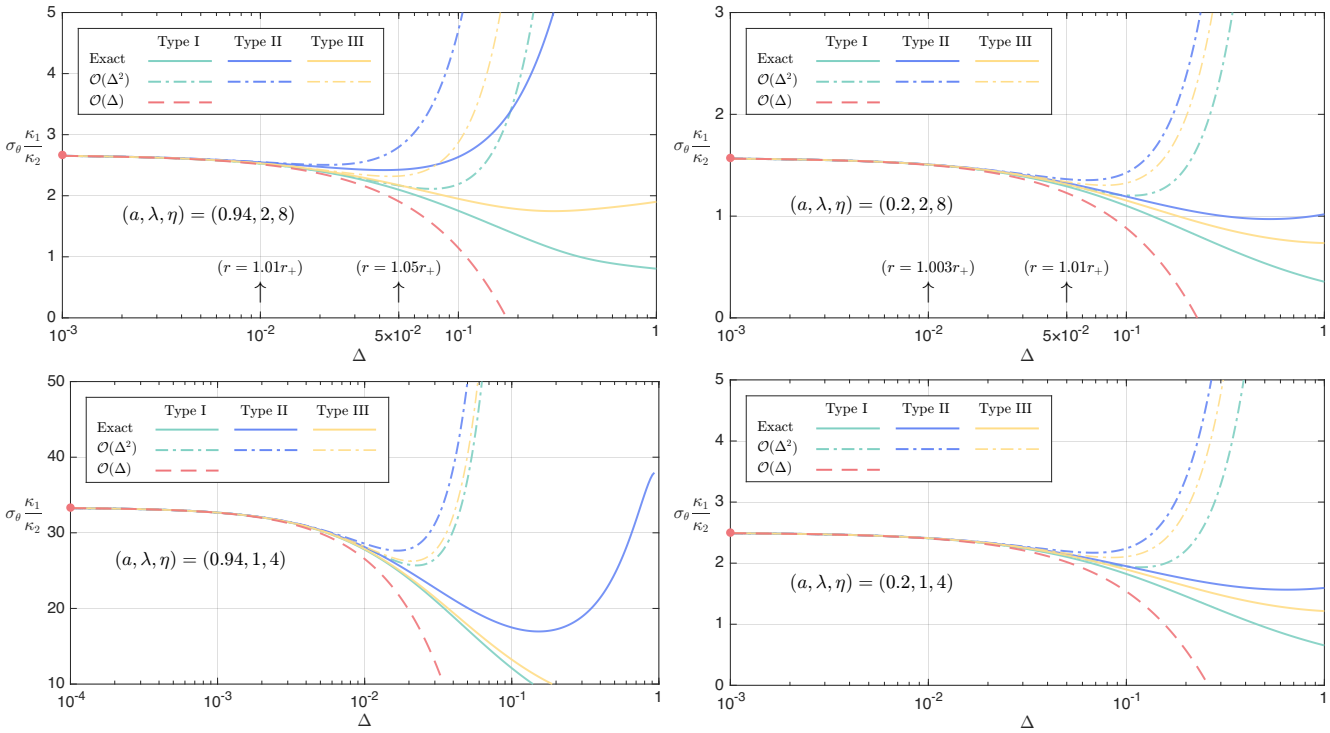

Figure 5. Compare the universal relationship of z with the exact z for the plasma under three different flow conditions. The field line angular velocity is set to $\Omega_B = 0$.

a sub-Keplerian inflow profile obtained from fitting GRMHD simulations in the MAD regime (A. Chael et al. 2021). The corresponding angular momentum density profiles are given by

$$l(r) \equiv -\frac{u_\phi}{u_t} = \begin{cases} 0\,, & \text{type I} \\ \dfrac{L_{\rm ms}}{E_{\rm ms}}, & \text{type II} \\ l_{\rm ms}\sqrt{\dfrac{r}{r_{\rm ms}}}\,, & \text{type III} \end{cases}, \tag{B2}$$

where $E_{\rm ms}$, $L_{\rm ms}$, and $r_{\rm ms}$ denote the conserved energy, angular momentum, and radius, respectively, of particles orbiting at the prograde ISCO,

$$\begin{aligned} r_{\rm ms} &= 3 + Z_2 - \sqrt{(3 - Z_1)(3 + Z_1 + 2Z_2)}\,, \\ Z_1 &= 1 + (1 - a^2)^{1/3}[(1 + a)^{1/3} + (1 - a)^{1/3}], \\ Z_2 &= \sqrt{3a^2 + Z_1^2}\,, \\ E_{\rm ms} &= \sqrt{1 - \frac{2}{3r_{\rm ms}}}\,,\ L_{\rm ms} = 2\sqrt{3}\left(1 - \frac{2a}{3\sqrt{r_{\rm ms}}}\right). \end{aligned} \tag{B3}$$

For accreting plasma of type III, the radial inflow velocity is modeled by a broken power-law fitting function, motivated by simulation results (A. Chael et al. 2021):

$$v_r \equiv \frac{u_r}{u_t} = v_{\rm ms}\left(\frac{r}{r_{\rm ms}}\right)^{-6}\left[\frac{1}{2} + \frac{1}{2}\left(\frac{r}{r_{\rm ms}}\right)^5\right]^{4/5}. \tag{B4}$$

To achieve the best agreement with the numerical results, the free parameters are set to $l_{\rm ms} = 1$, $v_{\rm ms} = 2$. It is worth noting that the inflow modes described above satisfy $Y = u_t + \Omega_H u_\phi < 0$, which is a necessary criterion for accretion to occur.

The influence of the inflow mode is encapsulated in the second term of Equation (B1). Therefore, to assess its impact, it suffices to compare the values of z generated by the three inflow models in Equation (B2) with those predicted by the near-horizon expansion in Equation (10). This comparison can be carried out in two equivalent ways. The first approach is to directly compare the near-horizon expansion, $z_0(a, \theta_o, \alpha, \beta) + \Delta z_1(a, \theta_o, \alpha, \beta, \Omega_B)$, with the full values of $z(a, \theta_o, \alpha, \beta, \Omega_B, u^\mu)$ computed from different inflow models across image planes with varying inclination angles, black hole spins, and field line angular velocities. In the polar coordinates (ρ, φ), the convergence of Equation (10) can be quantified by $\delta\rho \equiv \rho - \rho_+(\varphi)$, where $\rho_+(\varphi)$ denotes the angular radius of the projected event horizon.

Alternatively, since the mapping between $\{\lambda, \eta, \Delta\}$ and $\{\alpha, \beta\}$ is smooth and invertible outside the black hole for arbitrary values of a and θ_o, the comparison can equivalently be performed at the emission point. By varying the emission direction λ, η freely—without imposing constraints on the number or location of observers—one can directly compare the near-horizon expansion of z (Equation (10)) with the corresponding values derived from different inflow models. This method is more computationally convenient and enables a broader exploration of parameter space. Consequently, in the subsequent analysis, we focus on comparing z at the emission point. We have verified that the near-horizon expansion converges well with several representative emission directions, effectively capturing the overall convergence behavior of the NHP formula across the image plane. In what follows, we present results for two representative sets of impact parameters: $(\lambda, \eta) = (2, 8)$ and $(1, 4)$.

In Figure 5, we compare the near-horizon expansion given by Equation (10) with the exact values of z computed under the three inflow models, with the field line angular velocity fixed at $\Omega_B = 0$. The top row of Figure 5 corresponds to photons

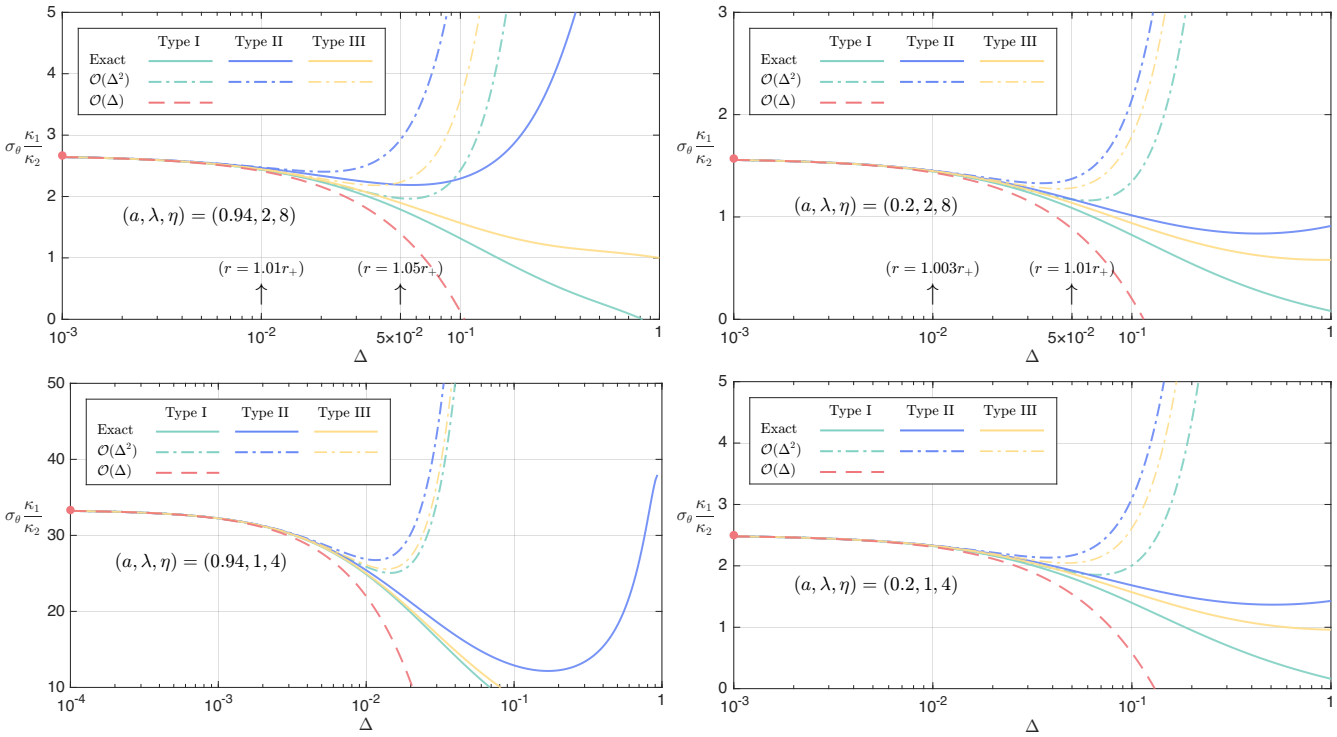

Figure 6. Compare the universal relationship of z with the exact z for the plasma under three different flow conditions. The field line angular velocity is set to $\Omega_B = 0.5\Omega_H$.

emitted with impact parameters $(\lambda, \eta) = (2, 8)$. For a rapidly spinning black hole with $a = 0.94$, we find that the expansion up to next-to-leading order in Equation (10) agrees remarkably well with the exact result within the range $r = 1.01r_+$. Beyond $r = 1.05r_+$, the different inflow models begin to exhibit discernible deviations. In contrast, for a slowly spinning black hole with $a = 0.2$, the same expansion already introduces noticeable discrepancies at $r = 1.01r_+$, indicating a slower convergence rate in the low-spin regime. The bottom row of Figure 5 shows results for photons with $(\lambda, \eta) = (1, 4)$. In this case, the convergence radius for $a = 0.94$ is reduced compared to the $(\lambda, \eta) = (2, 8)$ case, while for $a = 0.2$, the convergence behavior remains largely unchanged.

Figures 1, 5, and 6, increasing Ω_B consistently leads to a reduction in the convergence radius of the near-horizon expansion. A quantitative understanding of this effect would require analyzing the influence of Ω_B on the next-to-next-to-leading-order terms, which lies beyond the scope of the present work.

For completeness, we provide a few useful expressions related to the NHP pattern. To visualize the NHP structure on the image plane, it is convenient to switch to polar coordinates, $\alpha = -\rho \sin\varphi$, $\beta = \rho\cos\varphi$. The corresponding relations for the impact parameters are $\lambda = \rho \sin\varphi \sin\theta_o$, $\eta = (\cos^2\varphi + \sin^2\varphi\cos^2\theta_o)\rho^2 - a^2\cos^2\theta_o$. The two leading terms in the near-horizon expansion of z are given by

$$
\begin{aligned}
z_0 =& \ \mathrm{sign}(\cos\theta_o) \\
&\times \frac{\sqrt{(\cos^2\varphi + \sin^2\varphi\cos^2\theta_o)\rho^2 - a^2\cos^2\theta_o}}{a - \rho\sin\varphi\sin\theta_o}, \\
z_1 =& \ \mathrm{sign}(\cos\theta_o)\Omega_H^2 \frac{(1 - a\Omega_B)}{(\Omega_H - \Omega_B)} \\
&\times \frac{(\rho^2 + a^2\sin^2\theta_o - 2a\rho\sin\varphi\sin\theta_o)\sqrt{(\cos^2\varphi + \sin^2\varphi\cos^2\theta_o)\rho^2 - a^2\cos^2\theta_o}}{2a^2(a - \rho\sin\varphi\sin\theta_o)^2(1 - \Omega_H\rho\sin\varphi\sin\theta_o)}.
\end{aligned}
\tag{B5}
$$

Figure 6 presents the same comparison as Figure 5, except with the field line angular velocity set to $\Omega_B = 0.5\,\Omega_H$. It is evident that the inclusion of a nonzero Ω_B does not qualitatively alter the behavior of z as a function of Δ across different parameter choices. However, as demonstrated in Accordingly, when assessing the validity of the near-horizon expansion, one examines the behavior of z as a function of the radial displacement $\delta\rho = \rho - \rho_+(\varphi, a, \theta_o)$, i.e., the distance from the projected event horizon $\rho = \rho_+(\varphi, a, \theta_o)$ along a given direction φ. In A. Chael et al. (2021), the authors

presented a semianalytic fit for the projected event horizon:

$$\rho_+(\varphi, a, \theta_o) \approx 2\sqrt{r_+} - \left(1 + \frac{1}{2}\cos^2\theta_o\right)\tan^{-1}(\cos\varphi\tan\theta_o)\,. \tag{B6}$$

The above formula is particularly accurate for observer inclination angles of less than 45°, where the projected event horizon deviates only mildly from a circle, and spin-induced asymmetries are not dominant. (It should be noted that in A. Chael et al. 2021, φ is defined as the angle relative to the α-axis.)

Appendix C
Explicit Expressions in the Small Inclination Angle Regime

For an on-axis observer with inclination angle $\theta_o = 0°$, observables on the image plane depend solely on the angular radius ρ, and the polarization pattern exhibits axial symmetry about the line of sight (the spin axis). In this symmetric configuration, the net EVPA satisfies the relation $2\chi_{\rm net}(\rho) = \beta_2(\rho)$, where $\beta_2(\rho)$ denotes the second azimuthal Fourier mode of the linear polarization at fixed angular radius (Event Horizon Telescope Collaboration 2021a, 2024a).

The observed polarization pattern arises from an interplay of several physical mechanisms, including the magnetic field structure, the plasma inflow mode, and the gravitational lensing. In the absence of plasma motion and gravitational effects on light propagation, a spinning black hole would produce a purely radial polarization pattern as seen by an on-axis observer. This stems from the fact that the emitted polarization vector is largely orthogonal to the local magnetic field, which, near the event horizon, adopts a perfectly toroidal configuration due to extreme frame dragging.

However, the relativistic motion of the accretion flow introduces significant modifications. The Lorentz boost from the plasma's comoving frame to the black hole frame induces aberration, causing the polarization vector of the emitted radiation to deviate from being strictly orthogonal to the magnetic field lines in the black hole frame. Simultaneously, frame dragging along photon trajectories leads to a nontrivial rotation of the polarization vector, a phenomenon commonly referred to as the gravitational Faraday effect (H. Ishihara et al. 1988).

In the near-horizon region, the aberration effect can be characterized by the spacetime geometry alone, as different inflow modes asymptotically converge to a universal toroidal structure, as shown in Equation (6). Together with the gravitational Faraday rotation, these two general relativistic effects imprint distinctive and robust signatures on the NHP pattern observed in the image plane. The leading-order net EVPA takes a particularly simple form, as derived from Equations (11)–(13),

$$\chi_{\rm net} = -\tan^{-1}\left(\frac{a}{\sqrt{\rho_+(a)^2 - a^2}}\right), \tag{C1}$$

where the angular radius of the projected event horizon is given approximately by the semianalytic fit in Equation (B6), $\rho_+(a) \approx 2\sqrt{r_+}$. Figure 7 illustrates the dependence of the net EVPA, as given by Equation (C1), on the black hole spin parameter, as seen by an on-axis observer. The net EVPA decreases monotonically with increasing spin, reflecting a transition in the polarization morphology from a purely radial pattern in the nonrotating limit ($a \to 0$ but nonzero, $\chi_{\rm net} \to 0$) to a clockwise spiral pattern in the extremal limit ($a \to 1$, $\chi_{\rm net} \approx -26.^{\circ}8$).

For a small but nonzero inclination angle, we introduce the parameter $u \equiv \sin\theta_o \ll 1$ to facilitate a perturbative expansion. In this limit, the impact parameters of light rays can be approximated as $\lambda = (\rho\sin\varphi)u$, $\eta \approx \rho^2 - a^2 + 2(a^2 - \rho^2\sin^2\varphi)u$. These expressions reveal a slight breaking of axial symmetry in the polarization pattern. For the leading-order EVPA, given by $\chi = -\tan^{-1}(\beta/\mu) + \tan^{-1} z_0$, we expand the net EVPA in powers of u, yielding

$$\chi_{\rm net}(\rho, \varphi) = -\tan^{-1}\frac{1}{z(\rho, \varphi)} - \left(\frac{a\cos\varphi}{\rho}\right)u - \left(\frac{a^2\sin 2\varphi}{2\rho^2}\right)u^2 + \mathcal{O}(u^3)\,, \tag{C2}$$

where $z(\rho, \varphi) \approx z_0 + \Delta(\rho, \varphi)\, z_1$, and z_0, z_1 can be expanded as

$$z_0 = \frac{\sqrt{\rho^2 - a^2}}{a} + \left(\frac{\rho\sqrt{\rho^2 - a^2}\sin\varphi}{a^2}\right)u + \left[\frac{a^4 + (2\rho^4 - 3a^2\rho^2)\sin^2\varphi}{2a^3\sqrt{\rho^2 - a^2}}\right]u^2 + \mathcal{O}(u^3)\,, \tag{C3}$$

$$f_\Omega^{-1}\, z_1 = \frac{\rho^2\sqrt{\rho^2 - a^2}}{2a^4} - \sin\varphi\,\frac{\rho\sqrt{\rho^2 - a^2}}{4a^5}[4a^2 - (5 - \sqrt{1 - a^2}\,\rho^2)]u + [(18 - a^2 - 6\sqrt{1 - a^2})\rho^4 + (a^4 - 40a^2 + 10a^2\sqrt{1 - a^2})\rho^2 + 4a^4(1 - \sqrt{1 - a^2})]\frac{\rho^2\sin^2\varphi}{8a^6\sqrt{\rho^2 - a^2}}u^2 + (7\rho^2 - 4\rho^2\cos 2\varphi - 2a^2)\frac{u^2}{4a^2\sqrt{\rho^2 - a^2}} + \mathcal{O}(u^3), \tag{C4}$$

with $f_\Omega = \Omega_H^2(1 - a\Omega_B)(\Omega_H - \Omega_B)^{-1}$. By retaining only the leading-order terms in Equation (C2), we take the limit $z \to z_0$, where the asymmetry in the polarization pattern arises from the $\mathcal{O}(u)$ contributions in Equations (C2) and (C3). For spin parameter $a = 0.94$ and inclination angle $\theta_o = 17°$, the maximal asymmetry occurs near $\varphi = -\pi/2, \pi/2$, where the difference in net EVPA reaches $\chi_{\rm net}(\pi/2) - \chi_{\rm net}(-\pi/2) \approx 30.^{\circ}72$, as

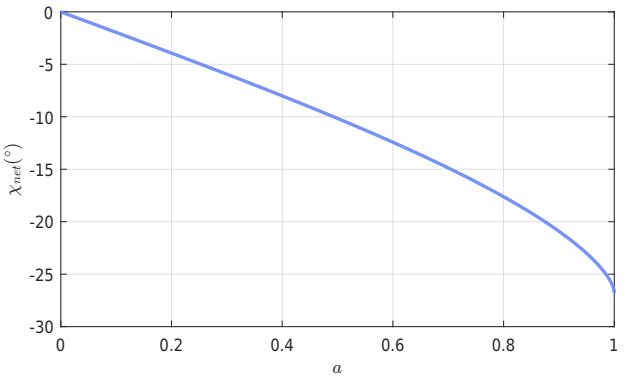

Figure 7. The net EVPA at the event horizon in the images of a Kerr black hole with varying spins, viewed by an on-axis observer. We have taken the modulus of $\chi_{\rm net}$ to bring it within the range of $[-\pi/2, \pi/2]$.

illustrated in Figure 3. By imposing $\rho = \rho_+$ in Equation (C2) and substituting the semianalytical fit for ρ_+, the behavior of the leading-order EVPA at small inclination angles can be fully determined. This explicit expression for the NHP pattern is particularly useful for constraining both the inclination angle and the black hole spin without degeneracy.

When the next-to-leading-order corrections are included, i.e., $z \approx z_0 + \Delta z_1$, it becomes necessary to establish the explicit mapping between the emission radius $r = r_+ + \delta r \approx r_+ + (r_+ - r_-)^{-1}\Delta$ and the angular radius ρ. For an on-axis observer, this mapping can be approximated via the following expansion (Z. Gelles et al. 2021):

$$r = \rho - 1 + \frac{1 - a^2}{2\rho} + \frac{3(5\pi - 16)}{4\rho^2} + \mathcal{O}(1/\rho^3)\,. \tag{C5}$$

Although Equation (C5) is formally derived in the asymptotic limit $r_s \gg 1$, it remains a good approximation even in the near-horizon regime, where $\delta r \ll 1$ (S. E. Gralla & A. Lupsasca 2020). In particular, to $\mathcal{O}(\rho^{-1})$ accuracy, Equation (C5) agrees remarkably well with the fitting formula $\rho_+ \approx 2\sqrt{r_+}$ proposed in A. Chael et al. (2021), with the relative deviation below 0.2%. This implies that, in the face-on case with $\theta_o = 0°$, either Equation (B6) or Equation (C5), accurate to $\mathcal{O}(\rho^{-1})$, can be reliably used to evaluate ρ_+.

Therefore, by combining Equations (C2), (C3), (C4), and (C5), one obtains an explicit expression for the near-horizon net EVPA accurate up to next-to-leading order. This result enables a direct and efficient analysis of the NHP pattern within a finite but small region outside the event horizon, rather than being restricted to the horizon itself.

Finally, it is important to emphasize that our analysis is applicable only to rotating black holes with nonzero spin. In the Schwarzschild case, the absence of frame dragging precludes both the development of an extreme toroidal plasma structure and the gravitational Faraday effect. Consequently, the polarization pattern in this case is governed by the inflow mode and the magnetic field configuration.

Appendix D
NHP in the KNTN Spacetime

In future work, we aim to investigate whether the characteristic features of the NHP pattern persist in more general rotating black hole spacetimes. As a representative example, we consider a multiparameter extension of the Kerr solution: the KNTN spacetime (J. B. Griffiths & J. Podolský 2009). We apply the near-horizon analysis developed earlier to examine the structure of the NHP in this more general context. Adopting the unit with $GM = c = 1$, the KNTN spacetime is characterized by three parameters: the spin parameter a, the electric charge Q, and the NUT charge l, the latter of which introduces a nontrivial topological structure and breaks asymptotic flatness. In Boyer–Lindquist coordinates, the line element is given by

$$\begin{aligned} ds^2 = &-\frac{1}{\tilde{\Sigma}}(\tilde{\Delta} - a^2\sin^2\theta)dt^2 + \frac{\tilde{\Sigma}}{\tilde{\Delta}}dr^2 + \tilde{\Sigma}d\theta^2 \\ &+ \frac{2}{\tilde{\Sigma}}[\tilde{\Delta}\mathcal{P} - a(\tilde{\Sigma} + a\mathcal{P})\sin^2\theta]dtd\phi \\ &+ \frac{1}{\tilde{\Sigma}}[(\tilde{\Sigma} + a\mathcal{P})^2\sin^2\theta - \mathcal{P}^2\tilde{\Delta}]d\phi^2, \end{aligned} \tag{D1}$$

where $\tilde{\Delta} = (r^2 - 2r + a^2 + Q^2 - l^2)$, $\tilde{\Sigma} = r^2 + (l + a\cos\theta)^2$ and $\mathcal{P} = a\sin^2\theta - 2\,l\cos\theta$. When $l = 0$, the spacetime reduces to the Kerr–Newman solution. For a nonzero NUT charge, however, the spacetime is no longer asymptotically flat; in particular, the off-diagonal metric component $g_{t\phi}$ asymptotically approaches $-2l\cos\theta$, reflecting the presence of a gravitomagnetic monopole. To ensure the existence of an event horizon, the spacetime parameters must satisfy the condition $a^2 + Q^2 \leqslant 1 + l^2$. The event horizon is located at the outer root of the equation $\tilde{\Delta} = 0$ and is given by

$$\tilde{r}_+ = 1 + \sqrt{1 - (a^2 + Q^2 - l^2)}\,. \tag{D2}$$

To analyze light propagation in the KNTN spacetime, we consider the rescaled photon four-momentum associated with the metric in Equation (D1). The energy-rescaled covariant four-momentum of a photon takes the form (V. P. Frolov & D. Kubizňák 2008; A. Grenzebach et al. 2014)

$$\begin{aligned} p_\mu dx^\mu &= -dt + \sigma_r\frac{\sqrt{\tilde{R}}}{\tilde{\Delta}}dr + \sigma_\theta\sqrt{\tilde{\Theta}}\,d\theta + \lambda d\phi\,, \\ \tilde{R} &= (r^2 + a^2 + l^2 - a\lambda)^2 - \tilde{\Delta}k\,, \\ \tilde{\Theta} &= k - \csc^2\theta(\lambda - a\sin^2\theta + 2l\cos\theta)^2\,, \end{aligned} \tag{D3}$$

where λ, η are conserved impact parameters and the constant k is defined as $k = \eta + (\lambda - a)^2$. Furthermore, since the KNTN spacetime is of Petrov type D, it admits a nontrivial Killing spinor, which guarantees the existence of a conserved Penrose–Walker constant. This constant governs the parallel transport of the polarization vector along null geodesics. The Penrose–Walker constant takes the form

$$\begin{aligned} &\kappa = \Xi(\mathcal{A} - i\mathcal{B}), \\ &\mathcal{A} = (p^t f^r - p^r f^t) + (a\sin^2\theta - 2l\cos\theta)(p^r f^\phi - p^\phi f^r), \\ &\mathcal{B} = [(r^2 + a^2 + l^2)(p^\phi f^\theta - p^\theta f^\phi) - a(p^t f^\theta - p^\theta f^t)]\sin\theta, \\ &\Xi = [r - i(l + a\cos\theta)]\left[-1 + il + \frac{Q^2}{r + i(l + a\cos\theta)}\right]^{-\frac{1}{3}}. \end{aligned} \tag{D4}$$

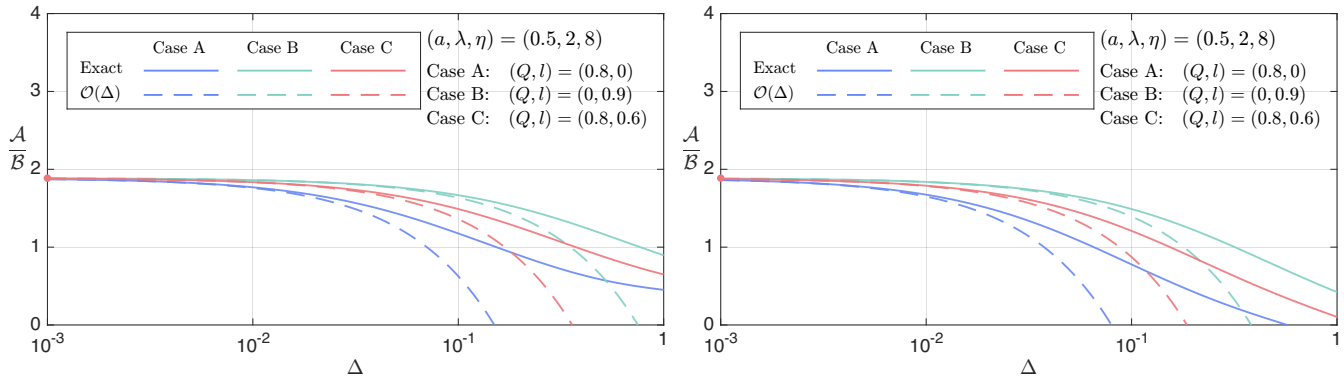

Figure 8. Comparison of the ratio $\mathcal{A}/\mathcal{B}$ up to the next-to-leading order in Equation (D5) with the exact value for a free-falling plasma under different black hole parameters in the KNTN spacetime, with $\Omega_B = 0$ (left) and $\Omega_B = 0.5\Omega_H$ (right). We have chosen $(a, \lambda, \eta) = (0.5, 2, 8)$.

Utilizing Equations (D3) and (D4), along with the general framework for an accreting magnetized plasma (Equations (2) and (3)), we compute the NHP in the KNTN spacetime in a manner analogous to that employed in the Kerr case. In the near-horizon limit $\Delta \to 0$, we expand the relevant physical quantities describing polarized radiation in powers of Δ. Following a series of systematic calculations (details omitted here), we find that the near-horizon expansion of the ratio $\tilde{z} \equiv -\mathcal{A}/\mathcal{B}$ at the emission point exhibits precisely the same functional form as that in the Kerr spacetime,

$$\tilde{z} = \frac{\sigma_\theta \sqrt{\eta}}{\lambda - a} + \left[\frac{(1 - a\Omega_B)}{(\Omega_h - \Omega_B)} \frac{\sigma_\theta\, \Omega_h^2\, k\, \sqrt{\eta}}{2a^2(\lambda - a)^2(\Omega_h \lambda - 1)}\right]\Delta + \mathcal{O}(\Delta^2)\,. \tag{D5}$$

Here, the angular velocity of the black hole horizon is given by $\Omega_h = a(r_h^2 + a^2 + l^2)^{-1}$. Clearly, in the above expansion, the leading-order term depends solely on the spacetime geometry and the conserved impact parameters. The next-to-leading-order correction further incorporates the field line angular velocity Ω_B, in addition to the spacetime geometry and impact parameters. Consequently, the resulting NHP pattern inherits the same qualitative features as in the Kerr spacetime: it is insensitive to the specific mode of plasma inflow and is governed only by the spacetime geometry and the magnetic field line rotation.

The expansion result in Equation (D5) is valid within the superradiant bound $\lambda \leqslant 1/\Omega_h$, which ensures that the energy of photons emitted near the horizon remains positive. We also note the presence of poles in the expansion at $\lambda = a$ and $\Omega_B = \Omega_h$, though a detailed analysis of these singularities is beyond the scope of this discussion. To assess the validity and convergence domain of the near-horizon expansion, we compare the analytic result from Equation (D5) with the exact numerical values of $\tilde{z}$ under a specific inflow mode, as shown in Figure 8. We see that the expansion, truncated at next-to-leading order in Δ, remains accurate within the regime $0 \leqslant \Delta \lesssim 10^{-1}$.

Next, we propagate the near-horizon emission to the observer's sky in order to explicitly determine the NHP pattern. Although the presence of the NUT charge renders the spacetime nonasymptotically flat, it is still possible to define a locally inertial observer by constructing an orthonormal tetrad at the distance. Following the standard procedure for setting up a locally nonrotating frame and defining photon arrival coordinates (C. T. Cunningham & J. M. Bardeen 1973), we introduce the coordinates (α, β) to parameterize the image plane,

$$\alpha = -\frac{\lambda}{\sin\theta_o}, \qquad \beta = \pm_\beta \sqrt{k - \csc^2\theta_o(\lambda - a\sin^2\theta_o + 2l\cos\theta_o)^2}\,, \tag{D6}$$

with θ_o being the observer's inclination angle. At large distances from the black hole, the radial component of the incoming photon's four-momentum dominates, satisfying $p^r \gg rp^\theta, rp^\phi$, and we can normalize the photon's four-momentum such that $-p_t = p^t = 1$, $p_r = p^r = 1$. The components of the polarization vector projected onto the image plane axes are then given by

$$f^\alpha_{(o)} = \frac{(f_{(o)})_\phi}{r_o \sin\theta_o} = r_o \sin\theta_o f^\phi_{(o)}\,, \quad f^\beta_{(o)} = -\frac{(f_{(o)})_\theta}{r_o} = -r_o f^\theta_{(o)}\,, \tag{D7}$$

where $r_o \gg 1$ denotes the radial coordinate of the distant observer. Imposing the orthogonality condition $p_\mu f^\mu = 0$ then yields $f^r = f^t - \beta f^\theta - \lambda f^\phi$. Hence, at the location of the distant observer, the Penrose–Walker constant simplifies to $\kappa = r_o(il - 1)^{-1/3}(\mathcal{A}_o + i\mathcal{B}_o)$,

$$\begin{aligned}\mathcal{A}_o &= -\beta f^\theta - \mu \sin\theta_o f^\phi \\ &= -\frac{1}{r_o}(\mu f^\alpha_{(o)} - \beta f^\beta_{(o)})\,, \\ \mathcal{B}_o &= \mu f^\theta - \beta \sin\theta_o f^\phi \\ &= -\frac{1}{r_o}(\beta f^\alpha_{(o)} + \mu f^\beta_{(o)})\,,\end{aligned} \tag{D8}$$

where $\mu = -(\alpha + a\sin\theta_o - 2l\cot\theta_o)$. The EVPA of the arriving photons is obtained through

$$\chi \equiv -\tan^{-1}\frac{f^\alpha_{(o)}}{f^\beta_{(o)}} = \tan^{-1}\left(\frac{\mu\tilde{z}_o - \beta}{\beta\tilde{z}_o + \mu}\right), \qquad \tilde{z}_o \equiv -\frac{\mathcal{A}_o}{\mathcal{B}_o}\,. \tag{D9}$$

Through Equation (D4), $(\mathcal{A}_o, \mathcal{B}_o)$ can be related to the near-horizon components $(\mathcal{A}, \mathcal{B})$ via a reflection matrix that

depends solely on the emission position and the observer's radius. Assuming the photon is emitted from the equatorial plane, this relation takes the form

$$\zeta_o \begin{pmatrix} \cos\delta_o & \sin\delta_o \\ \sin\delta_o & -\cos\delta_o \end{pmatrix} \begin{pmatrix} \mathcal{A}_o \\ \mathcal{B}_o \end{pmatrix} = \zeta \begin{pmatrix} \cos\delta & \sin\delta \\ \sin\delta & -\cos\delta \end{pmatrix} \begin{pmatrix} \mathcal{A} \\ \mathcal{B} \end{pmatrix}, \tag{D10}$$

where

$$\zeta_o = r_o(l^2+1)^{-\frac{1}{6}}, \quad \delta_o = \frac{\tan^{-1} l}{3},$$
$$\zeta = \sqrt{r^2+l^2}\left[\left(1-\frac{rQ^2}{r^2+l^2}\right)^2 + \left(l-\frac{lQ^2}{r^2+l^2}\right)^2\right]^{-\frac{1}{6}},$$
$$\delta = -\tan^{-1}\left(\frac{l}{r}\right) + \frac{1}{3}\tan^{-1}\left[\frac{l(r^2+l^2-Q^2)}{r^2-Q^2r+l^2}\right]. \tag{D11}$$

Therefore, combining Equations (D5), (D9), and (D10), we find that, to leading order in Δ, the NHP angle χ is independent of the plasma properties and instead purely encodes the spacetime geometry. This suggests that the polarization pattern near the horizon reflects intrinsic geometrical features of the spacetime and may be a universal characteristic of Petrov type D spacetimes. The polarization angle is given by

$$\chi = -\tan^{-1}\left(\frac{\beta}{\mu}\right) + \tan^{-1}\tilde{z}_o,$$
$$\tilde{z}_o = \frac{\tilde{z}\cos(\delta+\delta_o) - \sin(\delta+\delta_o)}{\tilde{z}\sin(\delta-\delta_o) - \cos(\delta-\delta_o)}. \tag{D12}$$

Finally, by substituting Equation (D5) into Equation (D12) and expanding δ in powers of Δ in Equation (D12), one can obtain the explicit near-horizon expansion of the EVPA in the KNTN spacetime. As the derivation is not particularly illuminating, we omit the detailed steps here.

ORCID iDs

Yehui Hou https://orcid.org/0000-0002-9434-3930
Jiewei Huang https://orcid.org/0009-0002-2360-2971
Minyong Guo https://orcid.org/0000-0001-5577-575X
Yosuke Mizuno https://orcid.org/0000-0002-8131-6730
Bin Chen https://orcid.org/0000-0003-4509-9705

References

Ayzenberg, D., Blackburn, L., Brito, R., et al. 2025, LRR, 28, 4
Bardeen, J. M. 1973, in Black Holes (Les Astres Occlus), ed. C. Dewitt & B. S. Dewitt, 215
Beckwith, K., & Done, C. 2005, MNRAS, 359, 1217
Blandford, R. D., & Payne, D. G. 1982, MNRAS, 199, 883
Blandford, R. D., & Znajek, R. L. 1977, MNRAS, 179, 433
Carter, B. 1968, PhRv, 174, 1559
Chael, A., Johnson, M. D., & Lupsasca, A. 2021, ApJ, 918, 6
Chael, A., Lupsasca, A., Wong, G. N., & Quataert, E. 2023, ApJ, 958, 65
Chael, A., Narayan, R., & Johnson, M. D. 2019, MNRAS, 486, 2873
Chandrasekhar, S. 1985, The Mathematical Theory of Black Holes (Oxford: Oxford Univ/ Press)
Compère, G., Liu, Y., & Long, J. 2022, PhRvD, 105, 024075
Cunningham, C. T., & Bardeen, J. M. 1973, ApJ, 183, 237
Dokuchaev, V. I., & Nazarova, N. O. 2020, PhyU, 190, 627
Emami, R., Ricarte, A., Wong, G. N., et al. 2023, ApJ, 950, 38
Event Horizon Telescope Collaboration 2019a, ApJL, 875, L1
Event Horizon Telescope Collaboration 2019b, ApJL, 875, L5
Event Horizon Telescope Collaboration 2019c, ApJL, 875, L6
Event Horizon Telescope Collaboration 2021a, ApJL, 910, L12
Event Horizon Telescope Collaboration 2021b, ApJL, 910, L13
Event Horizon Telescope Collaboration 2022a, ApJL, 930, L12
Event Horizon Telescope Collaboration 2022b, ApJL, 930, L16
Event Horizon Telescope Collaboration 2024a, ApJL, 964, L25
Event Horizon Telescope Collaboration 2024b, ApJL, 964, L26
Event Horizon Telescope Collaboration 2024c, arXiv:2410.02986
Frolov, V. P., & Kubizňák, D. 2008, CQGra, 25, 154005
Gelles, Z., Chael, A., & Quataert, E. 2025, ApJ, 981, 204
Gelles, Z., Himwich, E., Palumbo, D. C. M., & Johnson, M. D. 2021, PhRvD, 104, 044060
Gralla, S. E., & Lupsasca, A. 2020, PhRvD, 101, 044031
Gralla, S. E., Lupsasca, A., & Marrone, D. P. 2020, PhRvD, 102, 124004
Grenzebach, A., Perlick, V., & Lämmerzahl, C. 2014, PhRvD, 89, 124004
Griffiths, J. B., & Podolský, J. 2009, Exact Space-times in Einstein's General Relativity (Cambridge: Cambridge Univ. Press)
Hadar, S., Johnson, M. D., Lupsasca, A., & Wong, G. N. 2021, PhRvD, 103, 104038
Himwich, E., Johnson, M. D., Lupsasca, A., & Strominger, A. 2020, PhRvD, 101, 084020
Hou, Y., Zhang, Z., Guo, M., & Chen, B. 2024, JCAP, 2024, 030
Ishihara, H., Takahashi, M., & Tomimatsu, A. 1988, PhRvD, 38, 472
Jia, H., Quataert, E., Lupsasca, A., & Wong, G. N. 2024, PhRvD, 110, 083044
Johnson, M. D., Akiyama, K., Blackburn, L., et al. 2023, Galax, 11, 61
Johnson, M. D., Akiyama, K., Baturin, R., et al. 2024, Proc.SPIE, 13092, 130922D
Komissarov, S. S. 2004, MNRAS, 350, 407
Komissarov, S. S. 2005, MNRAS, 359, 801
Lockhart, W., & Gralla, S. E. 2022, MNRAS, 517, 2462
McKinney, J. C. 2006, MNRAS, 368, 1561
McKinney, J. C., Tchekhovskoy, A., & Blandford, R. D. 2012, MNRAS, 423, 3083
Medeiros, L., Chan, C.-K., Narayan, R., Ozel, F., & Psaltis, D. 2022, ApJ, 924, 46
Moscibrodzka, M., Dexter, J., Davelaar, J., & Falcke, H. 2017, MNRAS, 468, 2214
Narayan, R., Chael, A., Chatterjee, K., Ricarte, A., & Curd, B. 2022, MNRAS, 511, 3795
Narayan, R., Igumenshchev, I. V., & Abramowicz, M. A. 2003, PASJ, 55, L69
Palumbo, D. C. M. 2025, ApJL, 978, L4
Palumbo, D. C. M., Baubock, M., & Gammie, C. F. 2024, ApJ, 970, 151
Palumbo, D. C. M., Wong, G. N., & Prather, B. S. 2020, ApJ, 894, 156
Parfrey, K., Philippov, A., & Cerutti, B. 2019, PhRvL, 122, 035101
Petrov, A. Z. 1954, Uchenye Zapiski Kazanskogo Universiteta. Seriya Fiziko-Matematicheskie Nauki, 114, 55
Phinney, E. S., III 1984, PhD thesis, Univ. Cambridge
Qiu, R., Ricarte, A., Narayan, R., et al. 2023, MNRAS, 520, 4867
Ricarte, A., Palumbo, D. C. M., Narayan, R., Roelofs, F., & Emami, R. 2022, ApJL, 941, L12
Ricarte, A., Prather, B. S., Wong, G. N., et al. 2020, MNRAS, 498, 5468
Rybicki, G. B., & Lightman, A. P. 1979, Lightman Radiative Processes in Astrophysics (New York: Wiley)
Tchekhovskoy, A., Narayan, R., & McKinney, J. C. 2010, ApJ, 711, 50
Tchekhovskoy, A., Narayan, R., & McKinney, J. C. 2011, MNRAS, 418, L79
Thorne, K. S., & Macdonald, D. 1982, MNRAS, 198, 339
Vincent, F. H., Wielgus, M., Abramowicz, M. A., et al. 2021, A&A, 646, A37
Walker, M., & Penrose, R. 1970, CMaPh, 18, 265
Zhang, X. A., Ricarte, A., Pesce, D. W., et al. 2025, ApJ, 985, 41